CHAPTER-5

Synthesis, characterization, and OER activity of polypyrrole integrated $CoWO_4$ nanoparticles in alkaline solution

5.1. Abstract

A novel synthesized composite of cobalt tungstate ($CoWO_4$) and polypyrrole (ppy) was effectively developed by hydrothermal method, followed by in situ polymerization. The first time reported $CoWO_4$/ppy composite was characterized by implementing numerous physicochemical methods like XRD, XPS, HR-TEM, BET, and FT-IR. The further assessment of electrochemical performance was conducted through LSV, CV, EIS, and Tafel polarization measurements. The composite demonstrated significant catalytic activity for the alkaline water oxidation reaction (WOR), attaining an extremely low overpotential of 170 mV at a current density of 10 mA cm^{-2} (η_{10}) and a Tafel slope of 61 mV dec^{-1}. The values demonstrate a significant enhancement over the individual electrocatalytic performances of $CoWO_4$ and polypyrrole, highlighting the synergistic effect of the composite. The superior electrocatalytic activity of the composite material is further validated by its lowest charge transfer resistance (15 Ω) and standard energy of activation (18.57 kJ mol^{-1}), indicating enhanced electron transport and reduced energy barriers for the reaction. The research indicates that $CoWO_4$/ppy serves as a promising material for efficient electrocatalytic applications.

5.2. Introduction

An enormous amount of work has been put into creating a green energy alternative due to the world's ever-increasing energy needs, growing environmental concerns, and excessive usage of fossil fuels. Renewable energy sources like wind and solar electricity show promise, but installation and storage are expensive [1]. Electrochemical water splitting is widely regarded as a highly favorable strategy for achieving carbon neutral production of hydrogen and oxygen,

offering several advantages such as high purity of products, minimal CO_2 emissions, and the ability to store energy from constantly renewable sources like wind, and tidal power, solar photovoltaics, solar thermal [2].

In this regard, Efforts in research have largely centered around the oxygen evolution reaction (OER) and the hydrogen evolution reaction (HER), two pivotal steps in electrochemical water splitting, as viable means of creating sustainable energy like hydrogen fuel [3,4]. The water electrolysis process is impeded by OER, a sluggish kinetic process that must be improved [5]. OER hence necessitates the creation of an inexpensive and effective electrocatalyst, mostly based on the widely accessible and earth-abundant elements. Among the top performing electrocatalysts for the OER are noble metal oxides, especially RuO_2 and IrO_2 [6]. However, the lack of abundance and substantial cost of noble metal oxides highlight the necessity of developing affordable non-noble metal-based electrocatalysts with superior catalytic activity.

Numerous oxides based on 3d-transition metals have been created as OER electrocatalysts because of their distinctive electrical structure, abundance, and comparatively inexpensive cost [7–11]. Cobalt related substances have demonstrated themselves as being highly efficient electrocatalysts for overall water splitting because of their high stability, cost effectiveness, and strong catalytic activity towards OER [12,13]. Cobalt is a superior transition metal for electrocatalysis because of its redox potential, which is closer to the oxygen reduction range of water (E = 1.23 V vs. RHE) with multiple oxidation states (Co^{2+}/Co^{3+}) [14].

Tungsten has been shown to have the highest adsorption energy for hydrogen intermediates (H*) among earth-abundant transition metals, which means it can increase the

combining of H* to create H_2 in the HER [15]. According to certain research, tungsten-based OER electrocatalysts showed that tungsten might lower kinetic barriers in the OER process because of its high electron capture affinity [16,17]. Therefore, the bimetal combination based on cobalt and tungsten can improve the kinetics. Although it is still much less effective than RuO_2 or IrO_2, cobalt tungstate ($CoWO_4$) has recently demonstrated encouraging OER activity [18].

Since the discovery in the early 1900s, polypyrrole (ppy) has drawn much interest because of its special electrical characteristics, such as its high conductivity and stability, making it appropriate for various uses in sensors, electronics, and the biomedical industry [19]. Several synthesis techniques, including chemical oxidation and electrochemical deposition, may be used to customize the polymer's various morphologies, which include films, nanoparticles, and nanotubes [20]. When coupled with other materials, ppy has a synergistic effect in the context of electrocatalysis for the OER [21–23]. This improvement results from its capacity to serve as a conductive support, which raises the electrocatalysts' overall stability and charge transfer. The incorporation of ppy into electrocatalytic systems can lead to increased active surface area and facilitate the transport of ions and electrons, which are critical for efficient OER performance [19]. The exploration of ppy in OER applications highlights its potential as a versatile material that enhances catalytic performance and contributes to developing more sustainable energy technologies. As research continues to uncover its properties and interactions within composite materials, ppy stands out as a promising candidate for advancing electrocatalytic processes.

Through a hydrothermal technique and in situ polymerization, we have effectively created a $CoWO_4$/ppy composite by utilizing the exceptional catalytic properties of $CoWO_4$ and a conductive support polymer. The combination shows a strong synergistic impact and better catalytic activity than $CoWO_4$ and ppy components. Its crystalline integrity and distinct shape are confirmed by structural and morphological investigations. The strength of the composite is shown by its remarkable stability and endurance in alkaline solutions (1 M KOH). These results highlight the potential of readily available and cost-effective electrocatalysts and provide opportunities for additional research into cutting-edge materials for OER applications

5.3. Experimental

5.3.1. Materials

Sodium tungstate dihydrate ($Na_2WO_4 \cdot 2H_2O$) (AR, Merck, 99.9 %), pyrrole (AR, Merck, 99.9 %), cobalt chloride hexahydrate ($CoCl_2 \cdot 6H_2O$) (AR, Merck, 99.9 %), ferric chloride ($FeCl_3$) (AR, Merck, 99.9 %), sodium hydroxide (NaOH) (AR, Merck, 99.9 %). All the chemicals were applied just as they were delivered, without any further processing or refining.

5.3.2. Synthesis of Polypyrrole (ppy)

Polypyrrole was synthesized via oxidative polymerization using anhydrous ferric chloride ($FeCl_3$) as the oxidant. Initially, A total of 0.2 mL of pyrrole monomer was mixed into 50 mL of deionized water for dispersion under constant stirring to ensure uniform mixing. A 50 mL aqueous solution of 0.5 M of $FeCl_3$ was then added to the dispersion dropwise while maintaining uninterrupted stirring under a nitrogen environment. This will ensure the formation of uniform, porous ppy structures, that enhances surface area and charge transfer

efficiency. It also ensures good adhesion of ppy to $CoWO_4$, leading to efficient Fermi level tuning [10]. The reaction mixture was kept at a controlled temperature of 0–5 °C and allowed it to polymerize for 4 hours. An optimal reaction time of 3–6 hours ensures homogeneous, porous ppy layers, enhancing charge separation and electrochemical performance [24]. Also, polymerization at low temperatures (0–5 °C) promotes the formation of long, interconnected ppy chains with high conductivity and porous structures that enhance ion diffusion and charge mobility [25]. The resulting polypyrrole precipitate was filtered and repeatedly washed with deionized water and methanol until a neutral pH was achieved, ensuring unreacted materials and by-products were removed. Finally, the purified product was dried at 50 °C for 24 hours.

5.3.3. Preparation of $CoWO_4$

For the synthesis of $CoWO_4$, a solution of sodium tungstate (3.3 g, 0.1 mol) and cobalt chloride (0.893 g, 0.25 mol dissolved in 15 mL of deionized water) were prepared separately and combined under constant stirring. The resulting mixture exhibited a thick red color, and its pH was adjusted to 8 using a sodium hydroxide solution. The prepared solution was then loaded into a 50 mL Teflon-lined stainless-steel autoclave and heated hydrothermally at 160 °C for a duration of 24 hours. The obtained catalyst was thoroughly rinsed repeatedly with both deionized water and ethyl alcohol to eliminate contaminants and subsequently dried at 120 °C for 6 hours.

5.3.4. Preparation of $CoWO_4$/ppy composite

The $CoWO_4$/ppy composite was synthesized using a method similar to the procedure employed for polypyrrole synthesis. In this process, 0.5 g of the prepared $CoWO_4$ was introduced into

the reaction mixture before the initiation of the polymerization process, making the process unique and advantageous for catalyst development. The resulting composite was purified by washing thoroughly with distilled water, ethanol, and acetone multiple times to remove any impurities. The purified composite was then dried at 100 °C for 12 hours.

5.3.5. Electrode fabrication

The catalyst ink was formulated by suspending 1 mg of the catalyst in a blend of 20 µL deionized water, 40 µL ethanol, and 10 µL of 5 % Nafion. The dispersion was ultrasonicated for 1 hour to ensure uniform mixing. Subsequently, 60 µL of the prepared solution was drop-cast onto pre-cleaned fluorine-doped tin oxide (FTO) plates (1 × 1 cm^2 area). The coated plates were dried at room temperature and employed as the working electrode.

5.4. Characterizations

5.4.1. Physicochemical characterizations

The crystallinity of the fabricated catalysts was examined utilizing powder X-ray diffraction (XRD) on a Rigaku Smart Lab 9 kW diffractometer with a wavelength of 1.514 Å. The FT-IR spectra of prepared catalysts was characterized by ATR-FTIR (Bruker, ALPHA model) Spectrophotometer in the frequency range 500–4000 cm^{-1}. The morphology and microstructures of the prepared catalysts were looked through high-resolution transmission electron microscopy (HR-TEM) using a Thermo Fisher Technai 20 G^2. A K-alpha XPS device was used for the X-ray photoelectron spectroscopy (XPS) analysis for knowing the elemental composition and oxidation states of metals. Further, the specific surface area of a material is

calculated using the BET and the study was performed on N_2 adsorption desorption isotherm on Quantachrome Autosorb instrument.

5.4.2. Electrochemical characterizations

Electrochemical characterizations of the prepared catalysts were performed on CHI-608C instrument developed by CH Instruments, USA. The instrument facilitated the examination of cyclic voltammetry (CV), electrochemical impedance spectroscopy (EIS), and Tafel polarization, enabling comprehensive analysis. The aforementioned techniques were carried out as per established protocols described in previous studies [22,26]. The experiments used three electrode system in a Pyrex glass cell. The setup consists of a counter electrode, which was a circular platinum (Pt) foil, sourced from Aldrich, with a surface area of 8 cm^2 and a purity of 99.9 %. For the working electrode, a glass plate coated with fluorine-doped tin oxide (FTO) was utilized, featuring a surface area of 0.50 cm^2. A Hg/HgO reference electrode is used, immersed in a 1 M KOH electrolyte, to provide a stable reference potential for the electrochemical measurements. To establish a link between the electrolyte and reference electrode, a salt bridge containing agar-agar and KCl was used. All potential measurements contained within the study were cited to a Hg/HgO/1 M KOH reference electrode, which has a standard potential of 105.3 mV relative to the normal hydrogen electrode (NHE) [27]. To relate potential values measured by the Hg/HgO reference electrode to the reversible hydrogen electrode (RHE), **Equation 3.1** could be used which is already discussed in **Chapter 3**.

$$E_{RHE} = E_{Hg/HgO} + 0.0592 \times pH + E^{\circ}_{Hg/HgO} \qquad \textbf{(3.1)}$$

5.5. Results and discussion

5.5.1. Physicochemical characterizations

5.5.1.1. XRD analysis

The XRD pattern of the as-prepared materials is presented in **Figure 5.1**. At 2θ values of 15.5°, 18.9°, 23.7°, 24.6°, 30.6°, 36.3°, 38.4°, 41.2°, 44.3°, 45.7°, 52°, 53.9°, 61.7°, 65.1°, 68.6°, and 71.8°, the diffraction peaks for $CoWO_4$ were visible. These peaks matched with the monoclinic $CoWO_4$ crystal planes (010), (001), (−110), (011), (−111), (200), (002), (−201), (−211), (−112), (031), (−202), (−311), (−231), (−140), and (−312) respectively. Every diffraction peak matched with the typical JCPDS card number 15-0867 [28,29]. The slight shift in the peak corresponding to (-111) plane after the incorporation of ppy confirms the dispersion of ppy and not the intercalation over the $CoWO_4$ nanoparticles, as evident from the slight difference in the d spacing value (0.003 nm) [30]. The XRD pattern of the $CoWO_4$/ppy composite highlights the amorphous properties of ppy and the crystalline nature of $CoWO_4$. The broad hump in the range of 16° to 35° in the $CoWO_4$/ppy composite pattern is due to the amorphous nature of the ppy. The Debye-Scherrer equation **(Equation 3.2),** which is already discussed in **Chapter 3**, was utilized to ascertain the crystallite size (D) of the prepared catalysts.

$$D = \frac{k\lambda}{\beta \cos\theta} \qquad \textbf{(3.2)}$$

Where, the XRD wavelength is denoted by λ,

the full-width half maximum (FWHM) by β,

Bragg's angle by θ.

The fixed value of the crystal shape coefficient (k) is 0.89 [31].

The mean crystallite diameter has been discovered to be 19.41 nm for $CoWO_4$ and 19.62 nm for the composite material.

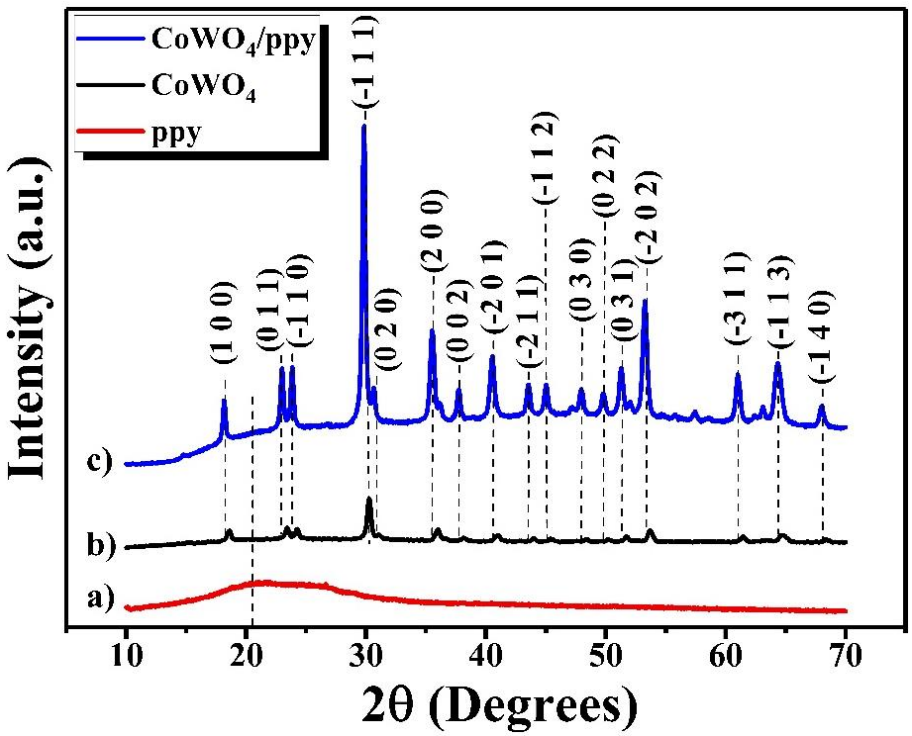

Figure 5.1. XRD patterns of **a)** ppy, **b)** $CoWO_4$, **c)** $CoWO_4$/ppy composite.

The slight increase in crystallite size can be attributed to the sample preparation process. The composite material was analyzed via XRD in the form of a thin film, which was heated at 70 °C for at least five hours. It is well known that temperature influences crystallite organization, leading to a marginal increase in crystallite size. To confirm this effect, we conducted XRD analysis of the composite material both before and after heating, as shown in **Figure 5.2** [32].

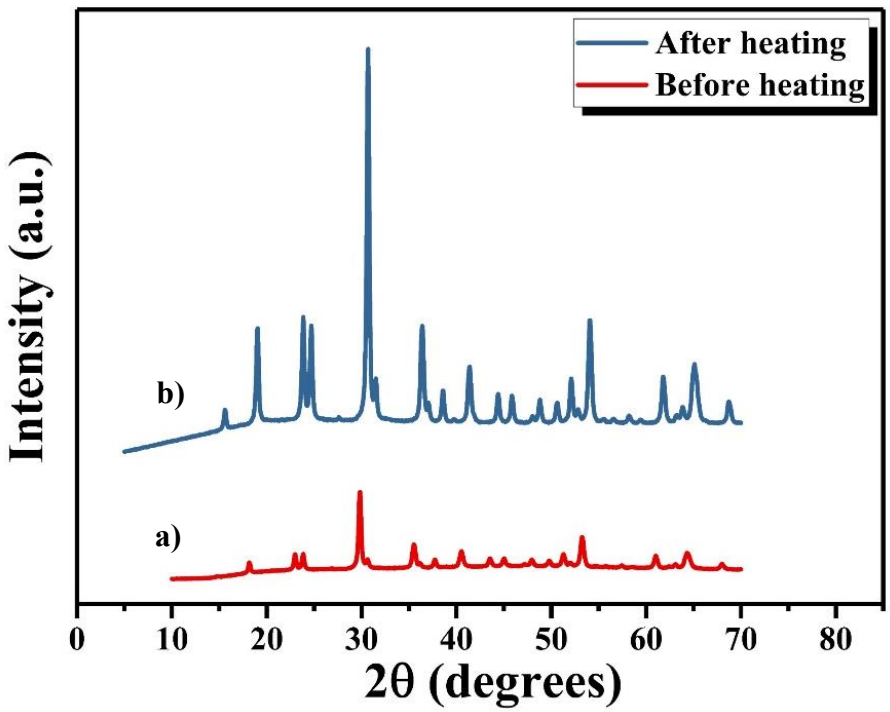

Figure 5.2. XRD patterns of $CoWO_4$/ppy composite material, **a)** before heating and **b)** after heating the sample.

5.5.1.2. FT-IR analysis

Figure 5.3 represents the FT-IR spectra of composite as well as pure $CoWO_4$. FT-IR confirms the incorporation of ppy in $CoWO_4$ as shown in the figure. In the 500–4000 cm^{-1} frequency range, tungsten states of type ABO_4 displayed distinctive stretching vibration bands. The well-defined broad band at 632 cm^{-1} was assigned to the stretching frequency of the Co-O-W mode, while the band at 817 cm^{-1} was attributed to the O-Co-W-O stretching vibration mode [33]. The peak at 1301 cm^{-1} is ascribed to the C-N stretching frequency and the intense peak at 1180 cm^{-1} is due to C-H in-plane stretching [34]. For ppy, the band at 1553 cm^{-1} corresponds to the antisymmetric stretching vibration of the C=C bonds in the pyrrole ring, while the band at 1460

cm^{-1} is linked to the symmetric stretching vibration of the same bonds. The stretching frequency of the O-H group due to the moisture, was attributed to the significant peaks at 3432 cm^{-1} and 1648 cm^{-1} in the $CoWO_4$ FT-IR spectra [35]. This indicates that the prepared samples retain the ability to absorb water molecules from the air, even after undergoing annealing treatment. Furthermore, the aliphatic C-H peak appeared at 2920 cm^{-1} [36].

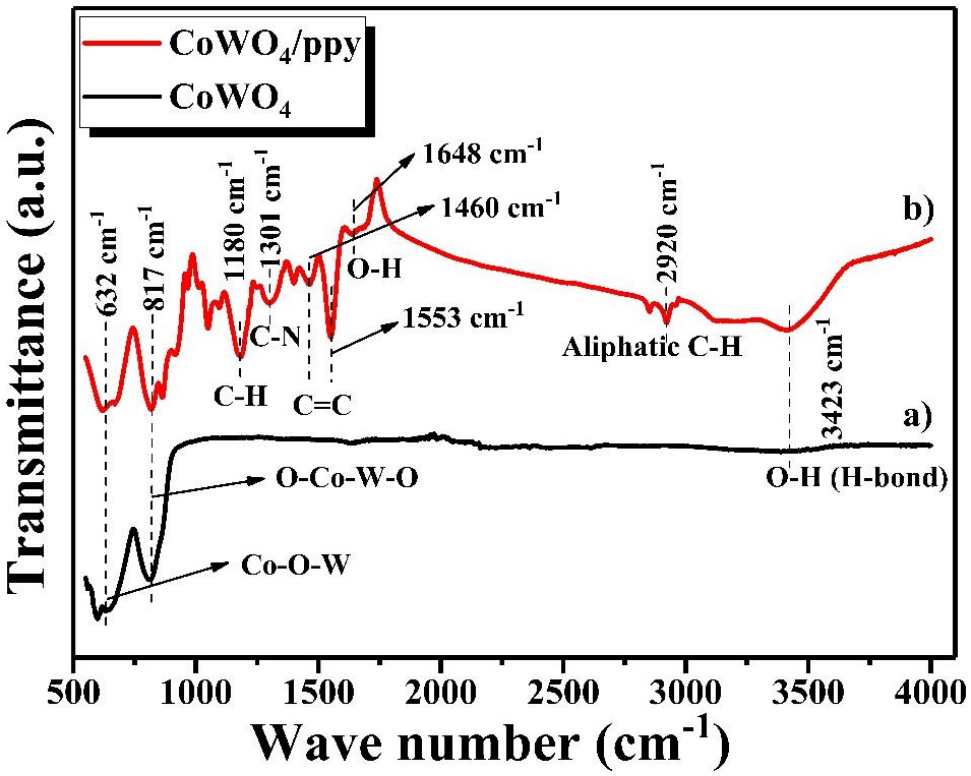

Figure 5.3. FT-IR of $CoWO_4$ and $CoWO_4$/ppy composite.

5.5.1.3. HR-TEM analysis

To probe the shape of $CoWO_4$/ppy, TEM study was performed. **Figure 5.4 (a)** and **(b)** display the TEM imaging of the sample at various magnifications. The shape of the nanoparticles is found to be distorted oval or cubic which has the ppy nano layer of 4.28 nm thickness encased

the $CoWO_4$ particles in the produced $CoWO_4$/ppy sample. The particle size is found to be in between 20 to 50 nm having an average particle size of 37 nm **(Figure 5.4 (e))**. **Figure 5.4 (b)** also showed close interaction between $CoWO_4$ and ppy. TEM scans showed that the $CoWO_4$/ppy composite was effectively produced by attaching ppy to the entire outer layer of $CoWO_4$. To confirm this, the TEM image of pristine $CoWO_4$, as shown in **Figure 5.5 (a)**, demonstrates the absence of any layering on the nanoparticles.

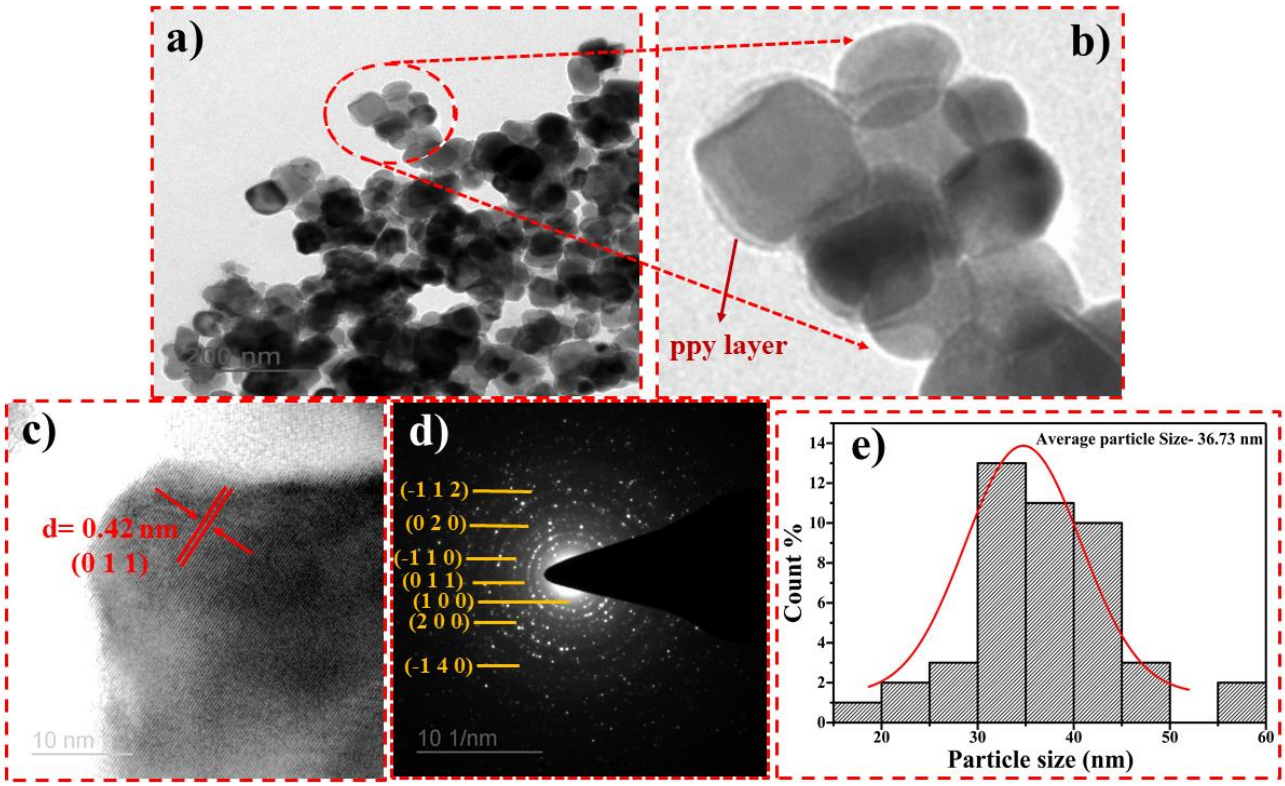

Figure 5.4. a) TEM micrograph of $CoWO_4$/ppy catalyst, **b)** magnified TEM micrograph of composite, **c)** HR-TEM micrograph of $CoWO_4$/ppy catalyst, **d)** SAED pattern of composite, **e)** Particle size distribution of composite.

A substantial amount of active surface area was expected to be provided by the $CoWO_4$/ppy structure connected to one another, enhancing the total quantity of active sites available to the electrolyte. Moreover, the microstructural observation reveals that the $CoWO_4$/ppy particles exhibit highly faceted morphologies, which generally arise from anisotropic crystal growth. Such faceted structures are advantageous as they expose more crystallographic active planes compared to unfaceted morphologies, thereby facilitating efficient adsorption and electron transfer during the OER process. Also, the d spacing measured from the lattice fringes found from the HR-TEM image **(Figure 5.4 (c))** is 0.35 nm that is proximal to the d spacing of (0 1 1) plane of monoclinic phase of the prepared catalyst. Moreover, the SAED pattern of $CoWO_4$/ppy nanocomposite reveals the well-defined rings, confirming its polycrystalline character **(Figure 5.4 (d))** [37]. These rings correspond to the crystal planes of monoclinic phase of composite material which is already indexed from the XRD analysis.

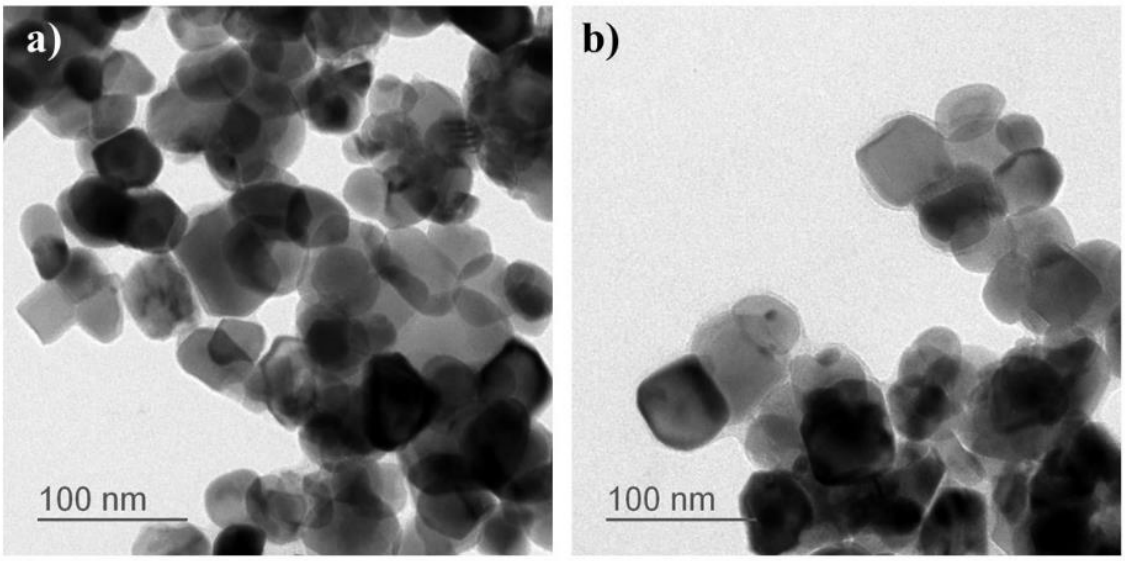

Figure 5.5. TEM micrographs of, **a)** pristine $CoWO_4$ and **b)** $CoWO_4$/ppy.

5.5.1.4. XPS analysis

XPS is a powerful analytical method for analyzing the composition and oxidation states of atoms in as-synthesized catalysts. The spectra provide detailed insights of the composition of the $CoWO_4$/ppy, identifying the existence of Co, W, N, C, and O as shown in **Figure 5.6. Figure 5.6 (a)** presents the core-level spectra of Co 2p. The two strong peaks observed at binding energies (B.E.) at 780.6 eV and 796.4 eV correlate with Co $2p_{3/2}$ and Co $2p_{1/2}$, respectively. These peaks arise from the spin-orbit coupling of the two terms and are characteristic of cobalt in the Co^{+2} oxidation state. Additionally, the satellite peaks observed at B.E. 786 eV and 803 eV further confirm the presence of cobalt oxide. Similar results are reported by S. Rajagopal *et al* [28]. For W 4f, as **(Figure 5.6 (b))** the two intense peaks observed at binding energies 34.68 eV and 36.86 eV correspond to W $4f_{7/2}$ and W $4f_{5/2}$, respectively. These peaks are characteristic of tungsten in the +6 oxidation state (W^{+6}) [28]. For O 1s, two strong bands at 529.9 and 531.9 eV are observed. The first one corresponds to the M-O bond for O^{2-} 1s and the latter one is for O_{vac}^{2-} 1s. This dual peak is common in catalysts consisting of metals in several oxidation states [26]. O_{vac}^{2-} ions are found in the oxygen-deficient region where the effective nuclear charge is slightly higher than that felt by electrons of 1s for O^{2-} ions in the M-O bond and hence appear at a little higher binding energy (2 eV) as shown in **Figure 5.6 (c)** [26,38]. Furthermore, for N 1s, the two peaks at 399 and 401 eV are ascribed to C-NH-C and =N-C **(Figure 5.6 (e))**, and for C 1s three peaks ascribed to O-C=O, C=O/C=N, and C-O/C-N at BE's 284.2 eV, 285.8 eV, and 288.1 eV, respectively **(Figure 5.6 (d))** [39,40]. The successful synthesis of the $CoWO_4$/ppy composite is confirmed by the

presence of Co, W, O, C, and N, along with structural and chemical validation from XRD and FT-IR analyses.

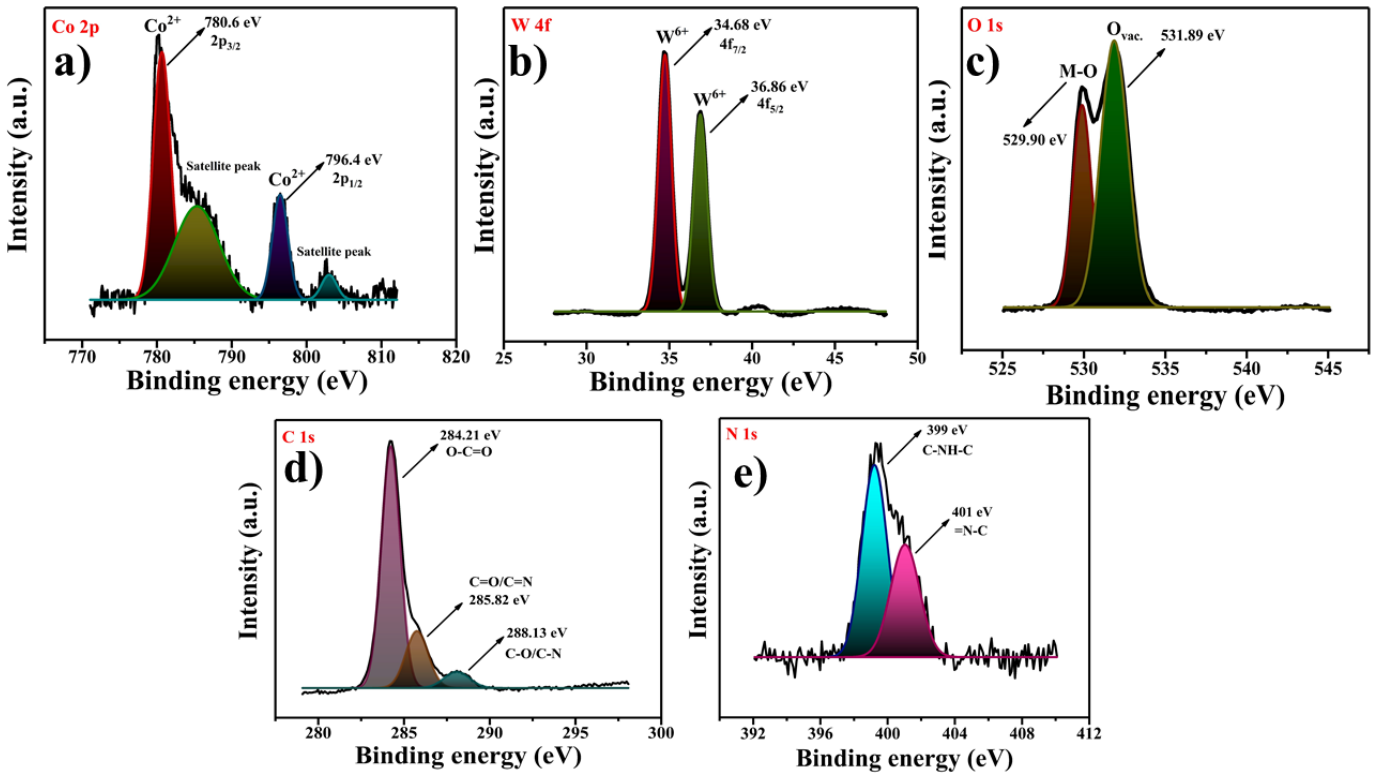

Figure 5.6. High resolution XPS spectra of **a)** Co 2p, **b)** W 4f, **c)** O 1s, **d)** C 1s, **e)** N 1s.

5.5.1.5. BET analysis

The textural properties, including surface area, pore volume, and pore-size distribution of the synthesized $CoWO_4$/ppy nanostructures, were systematically analyzed using the BET method. **Figure 5.7 (a)** presents the nitrogen adsorption–desorption isotherm recorded at 77 K, with the inset **(Figure 5.7 (b))** illustrating the corresponding pore size distribution curve obtained via the BJH model (Barrett-Joyner-Halenda model). The isotherm is classified as a Type IV

isotherm with H2-type hysteresis, which is characteristic of mesoporous materials. This observation suggests the presence of interconnected pore networks within the nanostructures, a feature that facilitates rapid ion transport and enhances electrochemical performance. The BJH pore size distribution curve further supports the mesoporous nature of the material, with pore sizes predominantly ranging from 2 to 40 nm [41]. The specific surface area of the $CoWO_4$/ppy nanostructures was determined to be 12.8 $m^2 g^{-1}$, while the average pore diameter was found to be 30.05 nm. Additionally, the total pore volume was measured to be 0.1061 $cm^3 g^{-1}$. These textural parameters indicate that the synthesized nanostructures possess a well-developed porous architecture. The presence of a high surface area coupled with a mesoporous structure is particularly advantageous for electrochemical applications, as it ensures a greater number of active sites for charge transfer and facilitates efficient electrolyte penetration [42]. This, in turn, can significantly improve the electrochemical performance by enhancing ion diffusion and charge transfer kinetics.

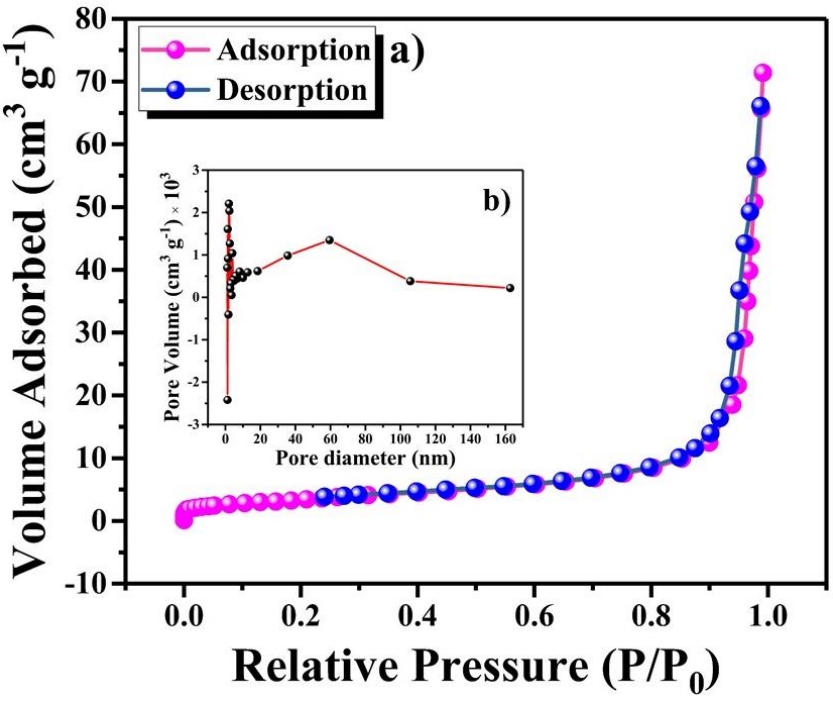

Figure 5.7. a) The gas adsorption–desorption isotherm curve of $CoWO_4$/ppy and, **b)** inset shows the BJH plot for the porosity evolution of $CoWO_4$/ppy.

5.5.2. Electrochemical characterizations

5.5.2.1. OER study

In a 1 M KOH electrolyte, at ambient temperature, the electrocatalytic activity of ppy, $CoWO_4$, and $CoWO_4$/ppy nanoparticles for the OER was assessed. At scan rates of 20 mV s^{-1} for CV and 0.5 mV s^{-1} for LSV, measurements were performed within a positive potential window of 1.1 V to 2 V vs. RHE. **Figure 5.8 (a)** display the typical LSV curves for the prepared catalysts and bare FTO electrode. It clearly demonstrated that the nanocomposite material has the lesser overpotential of 170 mV for achieving 10 mA cm^{-2} (η_{10}) than the $CoWO_4$ nanoparticle **(Figure 5.8 (c))** and other catalysts which are previously reported in the literature **(Table 5.1)**. This

increase in electrocatalytic activity might be due to the increase in oxygen vacancies [26] which is already confirmed from the XPS data of the composite material **(Figure 5.6)** and $CoWO_4$ nanomaterial **(Figure 5.9)**.

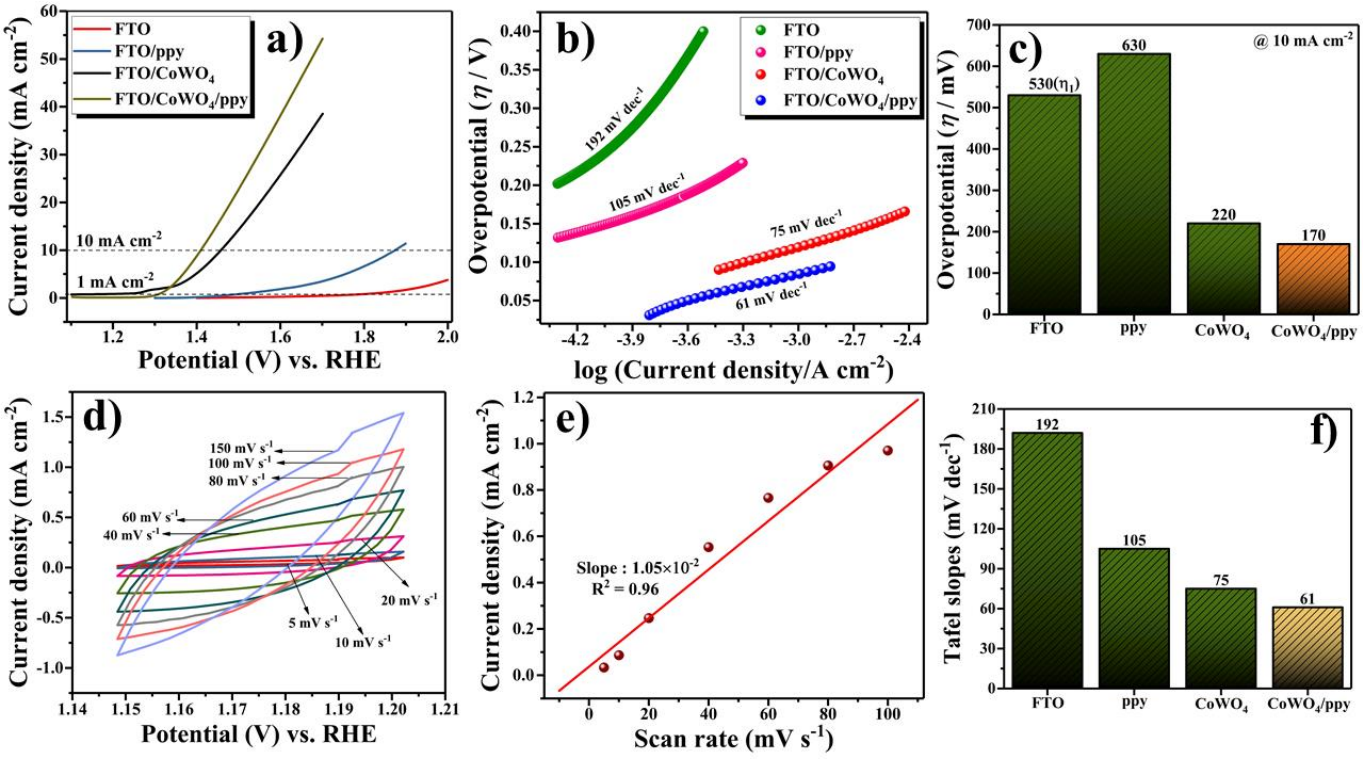

Figure 5.8. a) LSV of prepared catalysts along with bare electrode at 0.5 mV s^{-1} scan rate in 1 M KOH electrolyte at 25 ºC, **b)** Tafel slopes, **c)** Comparison of overpotential among the synthesized materials and the bare electrode, **d)** CV of FTO/$CoWO_4$/ppy electrode in non-faradaic region at varying scan rates, **e)** C_{dl} plot for FTO/ $CoWO_4$/ppy electrode **f)** Comparison of Tafel slopes among the synthesized materials and the bare electrode.

The importance of oxygen vacancies in improving the electrocatalytic efficacy of materials for the OER was emphasized by Liu *et al.* [43]. According to their research, enhanced

OER activity is closely correlated with a larger density of oxygen vacancies. This improvement is ascribed to the distinct electrical structure that the vacancies bring about, creating an environment on the catalyst surface that is rich in electrons. These vacancies' excess electrons improve the catalyst's interaction with adsorbed intermediates [44,45].

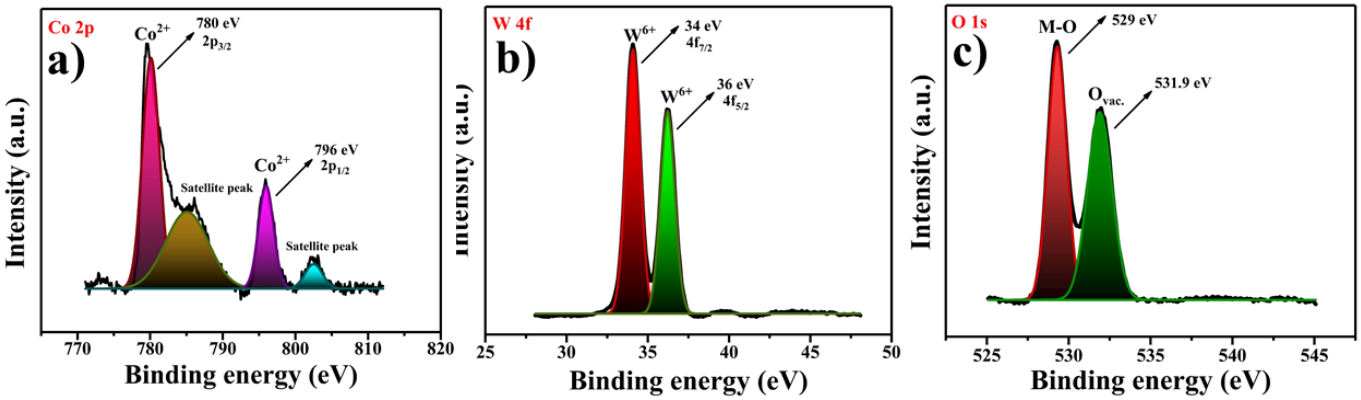

Figure 5.9. High resolution XPS spectra of **a)** Co 2p, **b)** W 4f, **c)** O 1s.

To ensure consistency in the material loading and surface roughness of the electrodes, the electrocatalytic functionality of the prepared samples was further investigated by determining both the specific current density (current per unit mass, **Equation 3.3**) and the true current density (current per unit of active surface area, **Equation 3.4**), as already discussed in **Chapter 3** [46]. By referring the CV **(Figure 5.10)**, three types of current densities, apparent (j_{app}), true (j_{true}), and specific (j_{spec}) were determined for composite material as well as for $CoWO_4$ **(Figure 5.11)**, and ppy **(Figure 5.12)**, for comparison, with the overpotentials corresponding to specified current densities. These results are summarized in **Table 5.2**.

The apparent and true current densities, normalized either by the geometric surface area of the electrode or the oxide roughness factor, provide valuable insights into the

electrochemical kinetics of oxygen evolution. Specifically, j_{app} reflects the overall activity based on the electrode's external surface area, while j_{true} accounts for the intrinsic activity by considering the actual electrochemically active area. Such normalization techniques are crucial for comparing catalytic performance across different systems and for gaining a deeper understanding of the underlying reaction mechanisms. The apparent current density (j_{app}) of the composite material is higher than that of pristine $CoWO_4$ due to the incorporation of polypyrrole (ppy), which increases the surface area and provides additional active sites for intermediate adsorption, thereby enhancing charge transfer efficiency. A similar trend is observed for the specific current density ($j_{specific}$). However, the true current density (j_{true}) is lower in the composite material, as it is normalized by the surface roughness, which is greater in the composite compared to pristine $CoWO_4$.

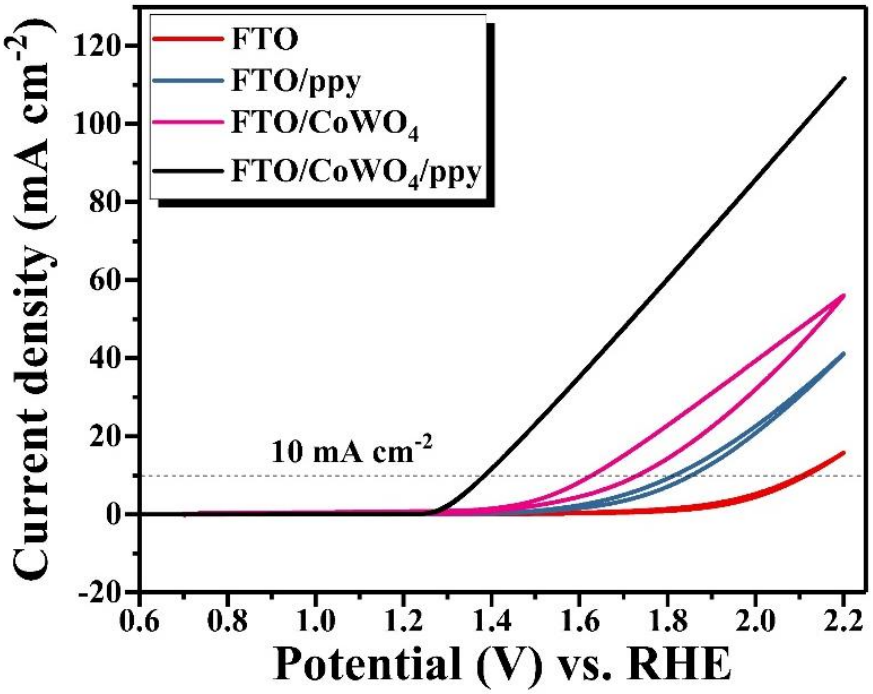

Figure 5.10. CV of prepared catalysts and bare electrode.

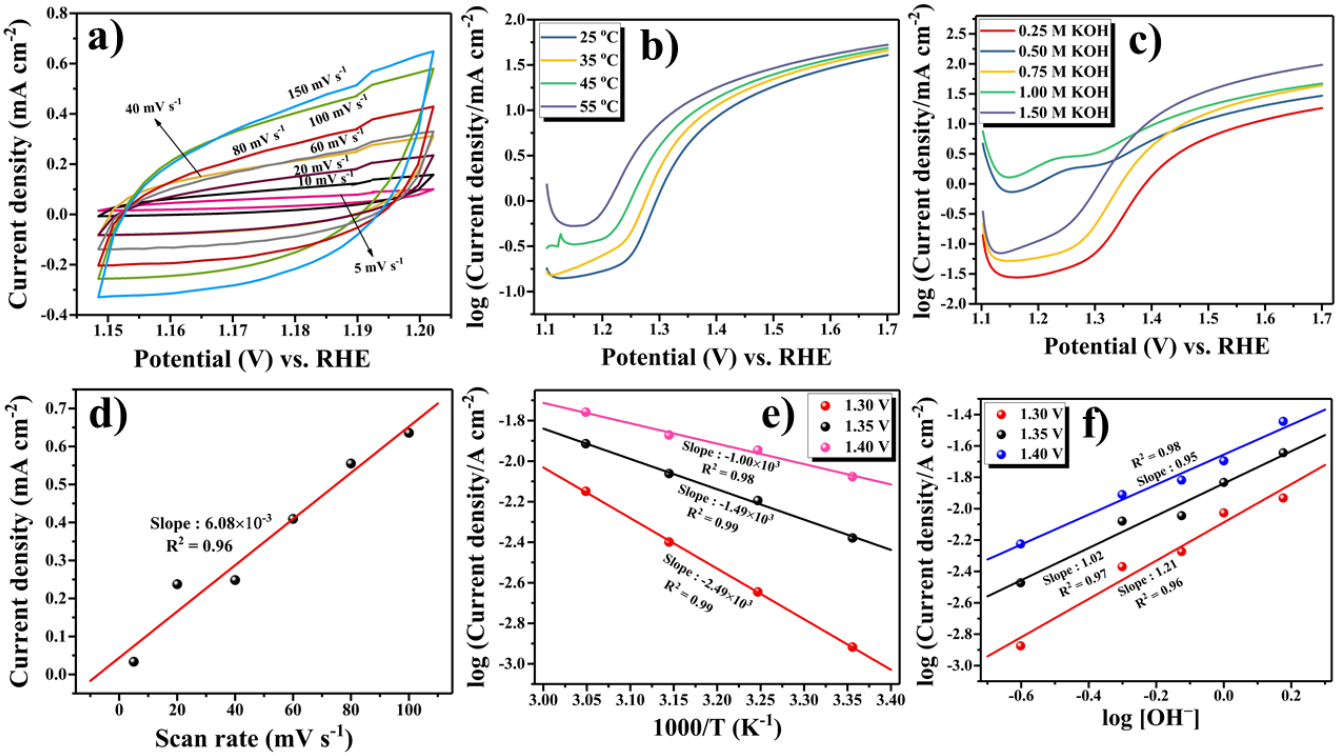

Figure 5.11. $CoWO_4$: a) CV in non-faradaic region at different scan rates, **b)** Tafel polarization curves at different temperatures, **c)** Tafel polarization curves at different concentrations of KOH, **d)** corresponding C_{dl} plot, **e)** corresponding Arrhenius plot, **f)** order of reaction.

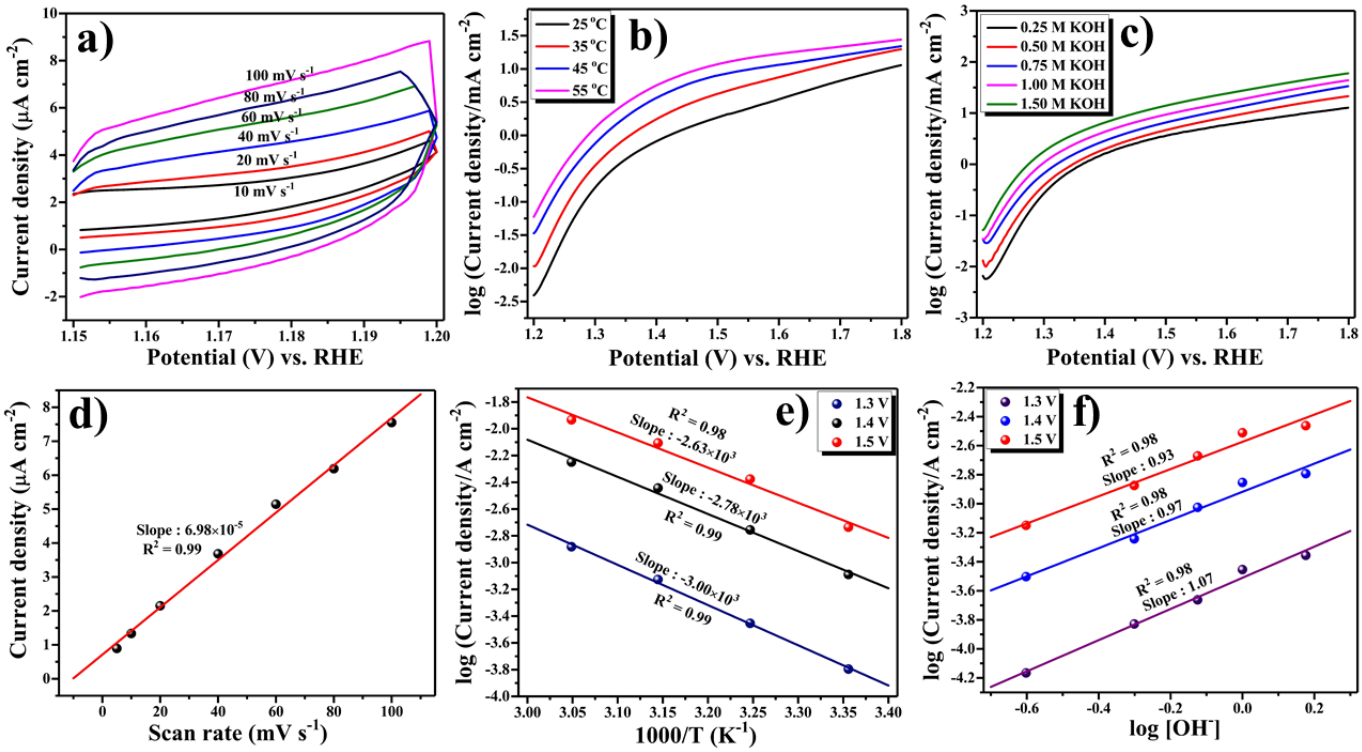

Figure 5.12. ppy: a) CV in non-faradaic region at different scan rates, **b)** Tafel polarization curves different temperatures, **c)** Tafel polarization curves at different concentrations of KOH, **d)** Corresponding C_{dl} plot, **e)** Corresponding Arrhenius plot, **f)** order of reaction.

Table 5.1. Comparison of various parameters of electrocatalytic OER for transition metal based and hybrid materials reported in the literature.

Material	**Overpotential (mV) / 10 mA cm^{-2}**	**Tafel slope / mV dec^{-1}**	**Electrolyte**	**References**
Co_3O_4/Co_2MnO_4	540	-	0.1 M KOH	[47]
$Mn_3O_4/CoSe_2$	450	49	0.1 M KOH	[48]
Co_6W_6C	343	72.6	1 M KOH	[49]
Porous Co_3O_4	460	89	0.1 M KOH	[50]
CoP hollow polyhedron	400	57	1 M KOH	[51]
ppy/ionic liquid	583	55	1 M KOH	[52]
$Co_{0.5}Mn_{0.5}WO_4$	400	84	0.1 M KOH	[53]
CoNiMn-LDH/ppy/rGO	369	77	1 M KOH	[54]
$ZnWO_4$	636	155	1 M KOH	[11]

$ZnWO_4$/ppy	507	84	1 M KOH	[55]
$NiWO_4$/Ni	363	-	1 M KOH	[56]
$CoWO_4$/ppy	170	61	1 M KOH	This work

Table 5.2. Electrode kinetic parameters

Electrode	**Overpotential (mV) at 10 mA cm^{-2}**	**Current density at E = 1.65 V (mA cm^{-2})**			**C_{dl} (mF cm^{-2})**	**R_f**	**ECSA (cm^2)**	**Tafel Slope (mV dec^{-1})**
		j_{app}	j_{true}	$j_{specific}$				
Bare	530 (ŋ1)	0.40	0.38	0.80	0.04	1.04	0.52	192
FTO/ppy	630	2.50	2.86	5.00	0.03	0.88	0.44	105
FTO/$CoWO_4$	220	38.47	0.51	76.94	3.04	76.00	38	75
FTO/$CoWO_4$/ppy	**170**	**46.35**	**0.35**	**92.70**	**5.25**	**131.25**	**65.62**	**61**

Figure 5.8 (b) presents the Tafel plots of the synthesized samples, offering valuable information about the OER kinetics of the catalysts. As observed, the Tafel slope of FTO/$CoWO_4$/ppy is 61 mV dec^{-1}, that is smaller than the $CoWO_4$ (75 mV dec^{-1}), and ppy (105 mV dec^{-1}). This lower Tafel slope indicates superior catalytic kinetics for composite material,

as a smaller slope corresponds to a faster electron transfer rate during the OER process **(Figure 5.8 (f))**. The improved performance of FTO/$CoWO_4$/ppy could be ascribed to its peculiar composition and framework, which synergistically enhance the active sites and optimize the interaction with intermediates involved in the OER mechanism. This least tafel slope and highest current density of composite is further explained by the Nyquist plots from EIS.

The double-layer capacitance (C_{dl}) was estimated through CV conducted in the non-faradaic potential range of 1.15 V to 1.20 V vs. RHE, at scan rates varying from 5 mV s^{-1} to 150 mV s^{-1} **(Figure 5.8 (d))**. A linear relationship was obtained by illustrating the scan rate against the current density **(Figure 5.8 (e))**. The slope of this line is measured to be 10.5 mF cm^{-2}. C_{dl} was then estimated as half the slope of this straight line, as described by **Equation 3.5 (Chapter 3)** [57]. Further analysis included determining the roughness factor (R_f) and the electrochemically active surface area (ECSA) of the catalysts, both critical parameters for assessing catalytic performance. The R_f, calculated using **Equation 1.25 (Chapter 1)** [58], provides insights into the distribution and accessibility of active sites within the catalyst. The ECSA, determined using **Equation 1.24 (Chapter 1)**, serves as a direct measure of the number of exposed active sites, which are vital for facilitating electron and proton transfer between the electrode and the electrolyte, as well as for driving the electrolysis process [59]. Among the studied catalysts, $CoWO_4$/ppy exhibited a significantly higher C_{dl} value of 5.25 mF cm^{-2} and an ECSA of 65.62 cm^2, outperforming the other materials **(Table 5.1)**. This elevated ECSA highlights the abundance of accessible active sites in composite, which enhances its catalytic efficiency by accelerating interfacial charge transfer processes. The combination of high C_{dl},

large ECSA, and favorable R_f underscores the potential of composite for high-performance catalytic applications.

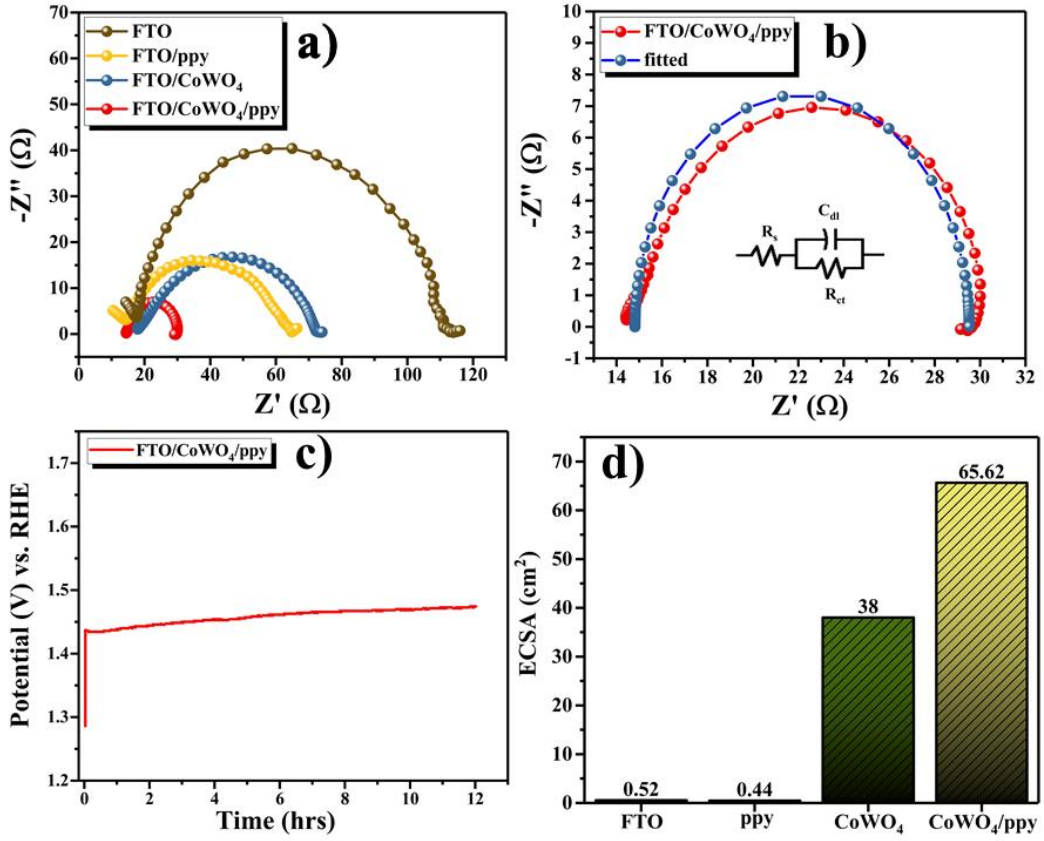

Figure 5.13. a) Nyquist plots of prepared catalysts and bare electrode at 1.3 V vs. RHE, **b)** Circuit fitted Nyquist plot of FTO/$CoWO_4$/ppy electrode, **c)** Chronopotentiometry stability test for FTO/$CoWO_4$/ppy electrode, **d)** Comparison of ECSA among the synthesized electrocatalysts and the bare electrode.

The EIS results align well with the LSV results, providing an in-depth understanding of the electrocatalytic efficiency of the substances under investigation. The Nyquist plot analysis was performed using an equivalent Randles circuit model, shown in the inset of

Figure 5.13 (b). This model incorporates key components: R_s, illustrating the solution resistance; and R_{ct}, which corresponds to the impedance to charge transfer at the interface between the electrode and electrolyte [60,61].

EIS was used to evaluate the charge transfer kinetics of adsorbed intermediates at the electrode-electrolyte interface [62]. This technique provides critical insights into the resistance and efficiency of charge transfer processes, which are key factors influencing the overall catalytic performance. A lower R_{ct} value reflects improved charge transfer efficiency, highlighting the effectiveness of the catalyst in facilitating electron movement between the active sites and the reactants. As depicted in **Figure 5.13 (a)**, the Nyquist plot from EIS reveals a semicircle formed at the onset potential of the OER. The EIS measurements were conducted with an amplitude of approximately 5.0 mV, spanning a frequency range from 100 kHz to 0.01 Hz, given an initial potential of 1.3 V vs. RHE. The obtained semicircle was analyzed using a Randle circuit model to extract key elements, that includes solution resistance (R_s) and charge transfer resistance (R_{ct}). The fitted results, presented in **Figure 5.13 (b)**, indicate that the R_{ct} value for $CoWO_4$/ppy is 15 Ω. The significantly lower R_{ct} value for $CoWO_4$/ppy than the $CoWO_4$ (48 Ω) and ppy (52 Ω) suggests that it exhibits superior charge transfer efficiency. This enhanced performance can be linked to the synergistic interactions within the $CoWO_4$/ppy composite, including the availability of a larger density of active sites at edges and the presence of oxygen bonds, which reduce the overpotential required for the OER. The reduced R_{ct} facilitates faster electron transfer, thereby improving the catalytic activity for OER.

5.5.2.2. Stability and durability

In many industrial and environmental processes, catalysts are essential because they allow for very efficient and selective chemical reactions. However, problems with stability and durability frequently limit their practical use. For catalytic systems to remain cost-effective and work well over the long run, certain characteristics are essential. To explore this characteristic, the stability and durability of the $CoWO_4$/ppy composite electrode was extensively assessed with chronopotentiometry in a 1 M KOH electrolyte solution. The chronopotentiometry shows a little increment in overpotential till few hours because the newly formed oxygen bubbles create resistance at the surface of the electrode and to overcome this resistance it needs some extra potential to achieve equilibrium [62,63]. Once equilibrium is reached, FTO/$CoWO_4$/ppy electrode displayed consistent durability, with less significant change in potential over the period of 12 hrs, as shown in **Figure 5.13 (c)**. The findings implied that, after achieving the equilibrium, the electrode's catalytic performance was unaffected by the gas bubble formation during the process, indicating its suitability for real-world applications. Continued advancements in this field will play a crucial role in meeting global energy, environmental, and economic challenges.

5.5.2.3. Thermodynamic Study

The prepared catalyst $CoWO_4$/ppy composite was thoroughly studied to evaluate essential thermodynamic parameters, including the standard activation entropy ($\Delta S^{0\neq}$), standard electrochemical activation energy ($\Delta H_{el}^{0\neq}$), and standard activation enthalpy ($\Delta H^{0\neq}$). Since these parameters are temperature-sensitive, the temperature was kept constant at 25 ^oC during

the entire study except for Tafel polarization curves for which the temperature range was 25 ^{o}C to 55 ^{o}C **(Figure 5.14 (a))** and corresponding Arrhenius plots are shown in **Figure 5.14 (b))**. The thermodynamic parameters for the catalysts have been compared and summarized in **Table 5.3**.

The $CoWO_4$/ppy composite has shown the lowest electrochemical energy of activation, and thus favors faster kinetics as per the Arrhenius equation, in comparison to its counterparts i.e. ppy and $CoWO_4$. Thus, the prepared composite serves as a more efficient electrocatalyst. Another parameter transfer coefficient (α), which measures the efficiency of electron transfer during the reaction, was evaluated using $\alpha=2.303RT/bF$, where, F is the Faraday constant, b is the tafel slope, T is the absolute temperature and R is the gas constant. The transfer coefficient for the composite material is maximum and found to be 0.96 **(Table 5.3)**, which is highest among the prepared catalyst defining its faster electron transfer efficacy.

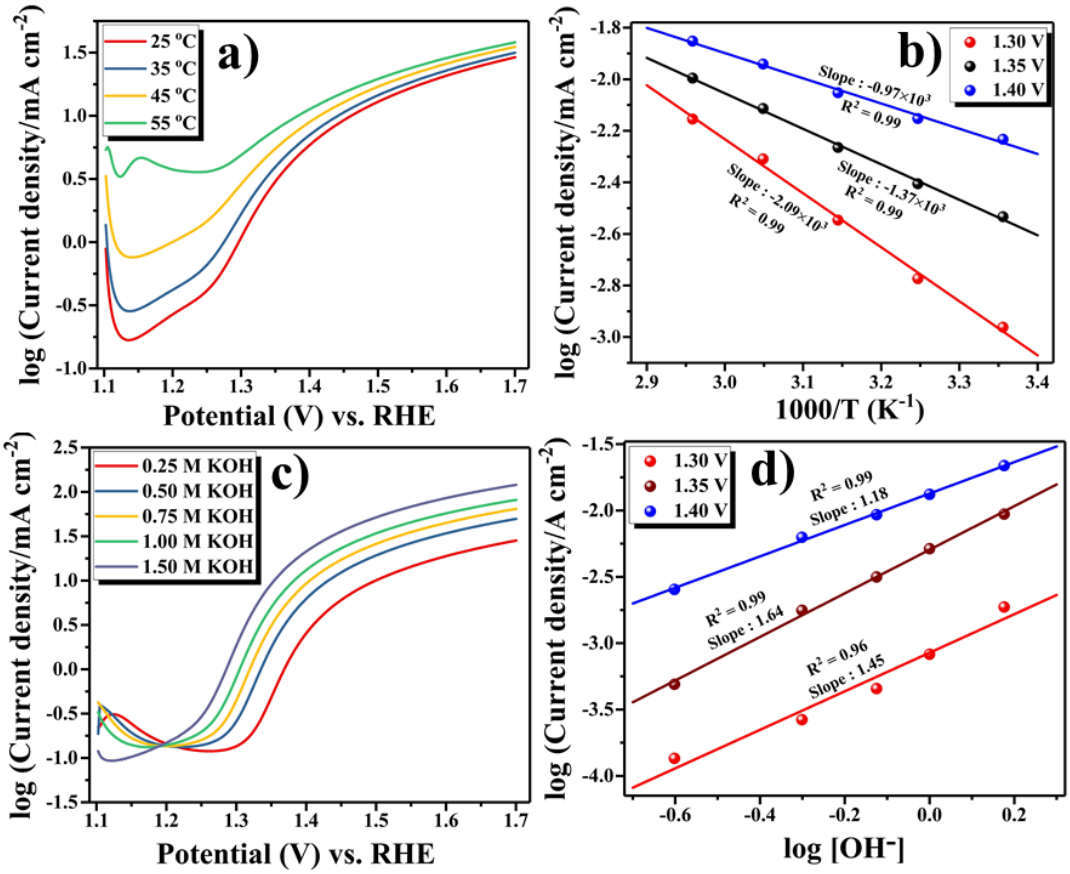

Figure 5.14. a) Tafel plots of FTO/$CoWO_4$/ppy electrode at increasing temperatures from 25 °C to 55 °C, **b)** Arrhenius plot, **c)** Tafel plots of FTO/$CoWO_4$/ppy electrode at varying concentrations of KOH **d)** order of reaction.

Thermodynamic parameters like $\Delta H^{0\neq}$ and $\Delta S^{0\neq}$ were calculated using the formulae from **Equations 1.28 and 1.30**, which is already discussed in **Chapter 1**. The earlier one gives an insight into the energy demand and the later one explains the degree of randomness during the transition state of the reaction. The standard electrochemical energy of activation ($\Delta H_{el}^{o\neq}$) and the standard enthalpy of activation ($\Delta H^{o\neq}$) provide insights into the energy required to drive the reaction. As evident from the data, both values are lower for the composite material,

indicating that it requires less energy to facilitate the reaction. Furthermore, the negative values of the standard entropy of activation ($\Delta S^{o\neq}$) confirm the occurrence of an adsorption process, as they reflect a decrease in system randomness. Notably, the composite material exhibits the most negative $\Delta S^{o\neq}$ value, further supporting this observation. In **Table 5.3**, the average of these quantities is given, illustrating the superior performance of the composite. Further, the Tafel slope (b) was calculated from anodic polarization plots at increasing temperatures. Finally, the frequency factor, calculated as k_BT/h, incorporates both Planck's constant (h) and the Boltzmann constant (k_B), and provides insight into the occurrence of effective collisions between reactants that result in the catalytic reaction.

Table 5.3. Thermodynamic parameters

Electrode	Standard electrochemical energy of activation ($\Delta H_{el}^{0\neq}$) (kJ mol^{-1})	Standard electrochemical entropy of activation ($-\Delta S_{el}^{0\neq}$) (J K^{-1}mol^{-1})	Transfer coefficient (α)	Standard enthalpy of activation ($\Delta H^{0\neq}$) (kJ mol^{-1})
Bare	58.02	52.82	0.31	63.07
FTO/ppy	53.23	28.14	0.56	62.47
FTO/$CoWO_4$	19.147	108.48	0.78	32.08
FTO/ $CoWO_4$/ppy	**18.57**	**114.65**	**0.96**	**34.47**

5.5.2.4. OER Mechanism

We initially determined the order of reaction for the produced samples employing various concentrations of KOH to gain insight into the OER mechanism [64]. This study uses a KNO_3 electrolyte to maintain a constant ionic strength of 1.5 while the concentration of OH^- ions was changed from 0.25 M to 1.25 M using KOH. Each concentration's Tafel polarization curves

were noted **(Figure 5.14 (c))**, and a graph was created by plotting the log (current density) against log [OH^-]. The resulting plot yielded a straight line, and as shown in **Figure 5.14 (d)**, the slope of this line reflects the reaction order.

The non-integral values obtained for the order of the reaction, occurring at the catalyst surface, have been a common observation as reported earlier [22,26]. This trend can be attributed to the interaction of OH^- ions with the catalyst surface, leading to the adsorption and ionization of hydroxyl groups in the process [65]. Furthermore, these non-integral values are also influenced by the overall surface saturation by adsorbed intermediates, including oxygen-based species produced during electrochemical oxygen evolution. This behavior affects the catalysts' performance throughout the reaction and happens under Temkin adsorption conditions, where, as surface coverage increases, the adsorption energy exhibits a linear decline [66].

The OER in basic medium is a crucial half-reaction in electrochemical energy conversion systems such as alkaline water electrolysis. It involves the oxidation of hydroxide ions (OH^-) to molecular oxygen (O_2) through a multi-step process, accompanied by the transfer of four electrons involving a single electron transfer at each stage. The incorporation of polypyrrole (ppy) enhances charge transfer kinetics, facilitating a more efficient electron transport process. This accelerated charge transfer subsequently promotes the rapid adsorption of reaction intermediates onto the active metal sites, thereby improving the overall electrocatalytic activity. The presence of ppy likely increases the electrical conductivity and modifies the electronic environment of the catalytic sites, leading to improved interaction between the catalyst surface and the reactive species. Consequently, this enhancement in

charge transfer and intermediate adsorption contributes to the superior catalytic performance of the composite material. The first step involves the adsorption of OH^- ions occurs at the active sites of the metal (Co/W), leading to electro-sorption as described in **Equation 5.1**. This process is accompanied with the development of an O=O bond via intermediates like OH^*, O^*, and OOH^*, that are adsorbed on the active sites, resulting in Co/W-O bonding **(Equations 5.2, 5.3, and 5.4)**. As a component of the OER process, these chemical steps have been thoroughly studied in the past [22,67,68].

$$OH^- + Co/W \rightarrow Co/W + OH^* + e^- \quad \textbf{(5.1)}$$

$$OH^* + OH^- \rightarrow O^* + H_2O + e^- \quad \textbf{(5.2)}$$

$$OH^- + O^* \rightarrow OOH^* + e^- \quad \textbf{(5.3)}$$

$$OH^- + OOH^* \rightarrow O_2 + H_2O + e^- \quad \textbf{(5.4)}$$

5.6. Conclusion

The novel $CoWO_4$/ppy composite was successfully synthesized through a hydrothermal method followed by in situ polymerization, and its structural and chemical properties were extensively characterized using HR-TEM, FT-IR, XRD, BET, and XPS. The comprehensive characterization confirmed the successful formation of the composite material and its unique properties that contribute to its enhanced performance. The electrocatalytic performance of the $CoWO_4$/ppy composite for the OER in 1 M KOH demonstrated significant improvements over its individual components, $CoWO_4$ and ppy. Under identical experimental conditions, the composite exhibited a notably lower Tafel slope, which is indicative of superior catalytic kinetics and a more efficient OER process. It is also noteworthy that the electrocatalytic

performance of the $CoWO_4$/ppy composite obtained in this work surpasses that of other similar ppy based hybrid materials reported in the literature. This improvement can be attributed to the synergistic interaction between $CoWO_4$ and the conductive ppy network, which facilitates efficient charge transfer, enhances structural stability, and provides a higher density of electrochemically accessible active sites. Such a combination results in superior OER activity compared to previously reported ppy based catalysts. Furthermore, the composite demonstrated almost first-order reaction kinetics with respect to OER, highlighting its effectiveness and the favorable interaction between $CoWO_4$ and ppy in promoting the reaction. The $CoWO_4$/ppy composite also exhibited excellent surface adherence to the FTO plate during stability tests, indicating its durability and long-term operational stability, which are critical for practical applications in energy conversion devices. These results collectively underscore the $CoWO_4$/ppy composite as a superior electrocatalyst for OER compared to its individual counterparts, showcasing both enhanced catalytic performance and long-term stability.

This study not only provides valuable perspectives on designing high-performance electrocatalysts for renewable energy applications but also opens avenues for the development of sustainable energy solutions. The enhanced performance and stability of the $CoWO_4$/ppy composite make it a promising candidate for use in future energy conversion technologies, contributing to the ongoing efforts to address global energy challenges and advance sustainable energy systems.

5.7. Reference

[1] A. Lewandowska-Bernat, U.D.-A. energy, undefined 2018, Opportunities of power-to-gas technology in different energy systems architectures, Elsevier (n.d.).

[2] W. Hao, R. Wu, R. Zhang, Y. Ha, Z. Chen, L. Wang, Y. Yang, X. Ma, D. Sun, F. Fang, Y. Guo, W. Hao, R. Wu, R. Zhang, Y. Ha, Z. Chen, X. Ma, D. Sun, F. Fang, Y. Guo, L. Wang, Y. Yang, Electroless plating of highly efficient bifunctional boride-based electrodes toward practical overall water splitting, Wiley Online Libr. Hao, R Wu, R Zhang, Y Ha, Z Chen, L Wang, Y Yang, X Ma, D Sun, F Fang, Y GuoAdvanced Energy Mater. 2018•Wiley Online Libr. 8 (2018). https://doi.org/10.1002/aenm.201801372.

[3] Y. Ma, X. Wang, Y. Jia, X. Chen, H. Han, C. Li, Titanium dioxide-based nanomaterials for photocatalytic fuel generations, Chem. Rev. 114 (2014) 9987–10043. https://doi.org/10.1021/cr500008u.

[4] F. Abdelghafar, X. Xu, S.P. Jiang, Z. Shao, Designing single-atom catalysts toward improved alkaline hydrogen evolution reaction, Mater. Reports Energy 2 (2022). https://doi.org/10.1016/j.matre.2022.100144.

[5] J. Song, C. Wei, Z.F. Huang, C. Liu, L. Zeng, X. Wang, Z.J. Xu, A review on fundamentals for designing oxygen evolution electrocatalysts, Chem. Soc. Rev. 49 (2020) 2196–2214. https://doi.org/10.1039/c9cs00607a.

[6] M. Guo, K. Xu, Y. Qu, F. Zeng, C. Yuan, Porous Co3O4/CoS2 nanosheet-assembled hierarchical microspheres as superior electrocatalyst towards oxygen evolution reaction, Electrochim. Acta 268 (2018) 10–19. https://doi.org/10.1016/j.electacta.2018.02.088.

[7] H. Sun, Z. Yan, F. Liu, W. Xu, F. Cheng, J. Chen, Self-Supported Transition-Metal-Based Electrocatalysts for Hydrogen and Oxygen Evolution, Adv. Mater. 32 (2020). https://doi.org/10.1002/adma.201806326.

[8] P. Chauhan, B. Lal, M. Malviya, A. Soni, Electrocatalytic Properties of Iron Ferrite (Fe3O4) Obtained by Thermal Decomposition Method Using Egg White (Ovalbumin), Russ. J. Electrochem. 59 (2023) 313–319. https://doi.org/10.1134/S1023193523040043.

[9] A. Soni, S.K. Maurya, M. Malviya, B. Lal, D. Tiwary, Evaluating Zn ferrite (ZnxFe3-xO4; $0 \leq x \leq 1$) for alkaline water oxidation: electrochemical and spectro-electrochemical study, J. Appl. Electrochem. (2024) 1–15. https://doi.org/10.1007/s10800-024-02164-2.

[10] N.H. Alotaibi, S. Manzoor, S. Saleem, S. Mohammad, M. Khalil, Ş. Yalçin, A.G. Abid, S.I. Allakhverdiev, Rational development of PPy/CuWO4 nanostructure as competent electrocatalyst for oxygen evolution, and hydrogen evolution reactions, Int. J.

Hydrogen Energy 59 (2024) 1326–1334. https://doi.org/10.1016/j.ijhydene.2024.02.125.

[11] K. Brijesh, K. Bindu, D. Shanbhag, H.S. Nagaraja, Chemically prepared Polypyrrole/ZnWO 4 nanocomposite electrodes for electrocatalytic water splitting, Int. J. Hydrogen Energy 44 (2019) 757–767. https://doi.org/10.1016/j.ijhydene.2018.11.022.

[12] Y. Sun, C. Liu, D.C. Grauer, J. Yano, J.R. Long, P. Yang, C.J. Chang, Electrodeposited cobalt-sulfide catalyst for electrochemical and photoelectrochemical hydrogen generation from water, J. Am. Chem. Soc. 135 (2013) 17699–17702. https://doi.org/10.1021/ja4094764.

[13] F. Song, W. Li, J. Yang, G. Han, T. Yan, X. Liu, Y. Rao, P. Liao, Z. Cao, Y. Sun, Interfacial sites between cobalt nitride and cobalt act as bifunctional catalysts for hydrogen electrochemistry, ACS Energy Lett. 4 (2019) 1594–1601. https://doi.org/10.1021/acsenergylett.9b00738.

[14] G. Arumugam, V. Murugesan, B. Chettiannan, S. Mathan, R. Rajendran, Multifunctional CoWO4 2D Array Electrode for Electrocatalytic Overall Water Splitting and Supercapacitor Application, Energy and Fuels 38 (2024) 5433–5448. https://doi.org/10.1021/acs.energyfuels.4c00091.

[15] N. Han, K. Yang, Z. Lu, Y. Li, W. Xu, T. Gao, … Z.C.-N., undefined 2018, Nitrogen-doped tungsten carbide nanoarray as an efficient bifunctional electrocatalyst for water splitting in acid, Nature.ComN Han, KR Yang, Z Lu, Y Li, W Xu, T Gao, Z Cai, Y Zhang, VS Batista, W Liu, X SunNature Commun. 2018•nature.Com (n.d.).

[16] L. Ding, K. Li, Z. Xie, G. Yang, S. Yu, W. Wang, H. Yu, J. Baxter, H.M. Meyer, D.A. Cullen, F.Y. Zhang, Constructing Ultrathin W-Doped NiFe Nanosheets via Facile Electrosynthesis as Bifunctional Electrocatalysts for Efficient Water Splitting, ACS Appl. Mater. Interfaces 13 (2021) 20070–20080. https://doi.org/10.1021/acsami.1c01815.

[17] Y. Zhu, G. Chen, Y. Zhong, W. Zhou, Z. Shao, Rationally Designed Hierarchically Structured Tungsten Nitride and Nitrogen-Rich Graphene-Like Carbon Nanocomposite as Efficient Hydrogen Evolution Electrocatalyst, Adv. Sci. 5 (2018). https://doi.org/10.1002/advs.201700603.

[18] B.J. Rani, G. Ravi, S. Ravichandran, V. Ganesh, F. Ameen, A. Al-Sabri, R. Yuvakkumar, Electrochemically active XWO4 (X = Co, Cu, Mn, Zn) nanostructure for water splitting applications, Appl. Nanosci. 8 (2018) 1241–1258. https://doi.org/10.1007/s13204-018-0780-2.

[19] D.D. Ateh, H.A. Navsaria, P. Vadgama, Polypyrrole-based conducting polymers and interactions with biological tissues, J. R. Soc. Interface 3 (2006) 741–752. https://doi.org/10.1098/rsif.2006.0141.

[20] L. Hao, C. Dong, L. Zhang, K. Zhu, D. Yu, Polypyrrole Nanomaterials: Structure,

Preparation and Application, Polymers (Basel). 14 (2022) 5139. https://doi.org/10.3390/polym14235139.

[21] H. Ai, L. Fan, Y. Wang, Z. Wang, H. Zhang, J. Zhao, M. Jiao, B. Lv, X. Han, OER catalytic performance of a composite catalyst comprising multi-layer thin flake Co3O4 and PPy nanofibers, RSC Adv. 13 (2023) 32045–32053. https://doi.org/10.1039/d3ra05936g.

[22] A. Soni, S. Kumar Maurya, M. Malviya, D. Tiwary, Exploring the synergistically enhanced activity of novel α-MnSe/ppy composite for superior OER catalyst in alkaline medium, J. Electroanal. Chem. 972 (2024) 118640. https://doi.org/10.1016/j.jelechem.2024.118640.

[23] S. Farid, W. Qiu, J. Zhao, X. Song, Q. Mao, S. Ren, C. Hao, Improved OER performance of Co3O4/N-CNTs derived from newly designed ZIF-67/PPy NTs composite, J. Electroanal. Chem. 858 (2020) 113768. https://doi.org/10.1016/j.jelechem.2019.113768.

[24] A. Kassim, Z.B. Basar, H.N.M.E. Mahmud, Effects of preparation temperature on the conductivity of polypyrrole conducting polymer, Proc. Indian Acad. Sci. Chem. Sci. 114 (2002) 155–162. https://doi.org/10.1007/BF02704308.

[25] M. Paúrová, I. Šeděnková, J. Hromádková, M. Babič, Polypyrrole nanoparticles: control of the size and morphology, J. Polym. Res. 27 (2020) 1–10. https://doi.org/10.1007/s10965-020-02331-x.

[26] S. Kumar Maurya, A. Soni, M. Malviya, D. Tiwary, Understanding the electrocatalytic role of magnesium doped bismuth copper titanate (BCTO) in oxygen evolution reaction, J. Electroanal. Chem. 975 (2024) 118803. https://doi.org/10.1016/j.jelechem.2024.118803.

[27] K. Kawashima, R.A. Márquez, Y.J. Son, C. Guo, R.R. Vaidyula, L.A. Smith, C.E. Chukwuneke, C.B. Mullins, Accurate Potentials of Hg/HgO Electrodes: Practical Parameters for Reporting Alkaline Water Electrolysis Overpotentials, ACS Catal. 13 (2023) 1893–1898. https://doi.org/10.1021/acscatal.2c05655.

[28] S. Rajagopal, D. Nataraj, O.Y. Khyzhun, Y. Djaoued, J. Robichaud, D. Mangalaraj, Hydrothermal synthesis and electronic properties of FeWO4 and CoWO4 nanostructures, J. Alloys Compd. 493 (2010) 340–345. https://doi.org/10.1016/j.jallcom.2009.12.099.

[29] V.K.V.P. Srirapu, A. Kumar, P. Srivastava, R.N. Singh, A.S.K. Sinha, Nanosized CoWO4 and NiWO4 as efficient oxygen-evolving electrocatalysts, Electrochim. Acta 209 (2016) 75–84. https://doi.org/10.1016/j.electacta.2016.05.042.

[30] R. Bissessur, P.K.Y. Liu, S.F. Scully, Intercalation of polypyrrole into graphite oxide, Synth. Met. 156 (2006) 1023–1027. https://doi.org/10.1016/j.synthmet.2006.06.024.

[31] S. Sagadevan, J. Podder, I. Das, Synthesis and characterization of CoWO4

nanoparticles via chemical precipitation technique, J. Mater. Sci. Mater. Electron. 27 (2016) 9885–9890. https://doi.org/10.1007/s10854-016-5057-5.

[32] S. Upadhyay, K. Parekh, B. Pandey, Influence of crystallite size on the magnetic properties of Fe3O4 nanoparticles, J. Alloys Compd. 678 (2016) 478–485. https://doi.org/10.1016/j.jallcom.2016.03.279.

[33] A. Ammasi, A.P. Munusamy, M. Shkir, F. Maiz, B. Vellingiri, V.R.M. Reddy, W.K. Kim, Synthesis and electrochemical performance of CoWO4 and CoWO4/MWCNT nanocomposites for highly efficient supercapacitor applications, Diam. Relat. Mater. 139 (2023) 110352. https://doi.org/10.1016/j.diamond.2023.110352.

[34] V. Keertheeswari Natarajan, S. Lakshmi Madaswamy, A. muteb Aljuwayid, M. Azam, S. Mohammad Wabaidur, R. Dhanusuraman, Ultrasound assisted synthesis of cobalt tungstate decorated Poly(2,5-dimethoxyaniline) nanocomposite towards improved methanol electro-oxidation, J. Ind. Eng. Chem. 121 (2023) 480–488. https://doi.org/10.1016/j.jiec.2023.02.003.

[35] X. Xu, J. Shen, N. Li, M. Ye, Facile synthesis of reduced graphene oxide/CoWO4 nanocomposites with enhanced electrochemical performances for supercapacitors, Electrochim. Acta 150 (2014) 23–34. https://doi.org/10.1016/j.electacta.2014.10.139.

[36] X. Wang, J. Deng, X. Duan, D. Liu, P. Liu, Fluorescent brightener CBS-X doped polypyrrole as smart electrode material for supercapacitors, Appl. Energy 153 (2015) 70–77. https://doi.org/10.1016/j.apenergy.2014.10.040.

[37] V.S. Rai, D. Prajapati, M.K. Verma, V. Kumar, S. Pandey, T. Das, N.B. Singh, K.D. Mandal, Influence of Zn doping on microstructure, dielectric, and electric properties in Bi2/3Cu3Ti4O12 ceramic synthesized by the semi-wet method, J. Mater. Sci. Mater. Electron. 33 (2022) 14868–14881. https://doi.org/10.1007/s10854-022-08405-4.

[38] X. Li, Y. Wang, W. Liu, G. Jiang, C.Z.-M. letters, undefined 2012, Study of oxygen vacancies′ influence on the lattice parameter in ZnO thin film, ElsevierX Li, Y Wang, W Liu, G Jiang, C ZhuMaterials Lett. 2012•Elsevier (n.d.).

[39] P. Muthukumaran, R. Ramya, P. Thivya, J. Wilson, G. Ravi, Nanocomposite based on restacked crystallites of β-NiS and Ppy for the determination of theophylline and uric acid on screen-printed electrodes, New J. Chem. 43 (2019) 19397–19407. https://doi.org/10.1039/c9nj04246f.

[40] A. Sathiyan, E. Elanthamilan, S.F. Wang, S. Dhineshkumar, J.P. Merlin, Fabrication of polypyrrole conductive matrix covered MnNi2O4 nanocomposite as a positive electrode material for asymmetric supercapacitor applications, New J. Chem. 48 (2024) 3080–3088. https://doi.org/10.1039/D3NJ05296F.

[41] M. Khalfaoui, S. Knani, M.A. Hachicha, A. Ben Lamine, New theoretical expressions for the five adsorption type isotherms classified by BET based on statistical physics treatment, J. Colloid Interface Sci. 263 (2003) 350–356. https://doi.org/10.1016/S0021-9797(03)00139-5.

[42] P.B. Patel, D. Patel, A.R. Patel, S.N. Bariya, Y.G. Kapdi, V. Solanki, S.S. Soni, M.H. Patel, Low-temperature synthesis of oval-shaped CoWO4 nanomaterials for enhanced asymmetric supercapacitor performance, Mater. Adv. 6 (2024) 726–742. https://doi.org/10.1039/d4ma00923a.

[43] S. Peng, F. Gong, L. Li, D. Yu, D. Ji, T. Zhang, Z. Hu, Z. Zhang, S. Chou, Y. Du, S. Ramakrishna, Necklace-like Multishelled Hollow Spinel Oxides with Oxygen Vacancies for Efficient Water Electrolysis, J. Am. Chem. Soc. 140 (2018) 13644–13653. https://doi.org/10.1021/jacs.8b05134.

[44] H. Li, S. Sun, S. Xi, Y. Chen, T. Wang, Y. Du, M. Sherburne, J.W. Ager, A.C. Fisher, Z.J. Xu, Metal-Oxygen Hybridization Determined Activity in Spinel-Based Oxygen Evolution Catalysts: A Case Study of ZnFe2- xCrxO4, Chem. Mater. 30 (2018) 6839–6848. https://doi.org/10.1021/acs.chemmater.8b02871.

[45] H. Zhu, P. Zhang, S. Dai, Recent Advances of Lanthanum-Based Perovskite Oxides for Catalysis, ACS Catal. 5 (2015) 6370–6385. https://doi.org/10.1021/acscatal.5b01667.

[46] A.S. Chaddha, N.K. Singh, M. Malviya, A. Sharma, Birnessite-clay mineral couple in the rock varnish: a nature's electrocatalyst, Sustain. Energy Fuels 6 (2022) 2553–2569. https://doi.org/10.1039/d2se00185c.

[47] D. Wang, X. Chen, D.G. Evans, W. Yang, Well-dispersed Co3O4/Co2MnO4 nanocomposites as a synergistic bifunctional catalyst for oxygen reduction and oxygen evolution reactions, Nanoscale 5 (2013) 5312–5315. https://doi.org/10.1039/c3nr00444a.

[48] M.R. Gao, Y.F. Xu, J. Jiang, Y.R. Zheng, S.H. Yu, Water oxidation electrocatalyzed by an efficient Mn3O 4/CoSe2 nanocomposite, J. Am. Chem. Soc. 134 (2012) 2930–2933. https://doi.org/10.1021/ja211526y.

[49] Z.Y. Yu, Y. Duan, M.R. Gao, C.C. Lang, Y.R. Zheng, S.H. Yu, A one-dimensional porous carbon-supported Ni/Mo2C dual catalyst for efficient water splitting, Chem. Sci. 8 (2017) 968–973. https://doi.org/10.1039/c6sc03356c.

[50] L. Li, T. Tian, J. Jiang, L. Ai, Hierarchically porous Co3O4 architectures with honeycomb-like structures for efficient oxygen generation from electrochemical water splitting, J. Power Sources 294 (2015) 103–111. https://doi.org/10.1016/j.jpowsour.2015.06.056.

[51] M. Liu, J. Li, Cobalt Phosphide Hollow Polyhedron as Efficient Bifunctional Electrocatalysts for the Evolution Reaction of Hydrogen and Oxygen, ACS Appl. Mater. Interfaces 8 (2016) 2158–2165. https://doi.org/10.1021/acsami.5b10727.

[52] A. Chinnappan, H. Bandal, S. Ramakrishna, H. Kim, Facile synthesis of polypyrrole/ionic liquid nanoparticles and use as an electrocatalyst for oxygen evolution reaction, Chem. Eng. J. 335 (2018) 215–220. https://doi.org/10.1016/j.cej.2017.10.108.

[53] G. Karkera, T. Sarkar, M.D. Bharadwaj, A.S. Prakash, Design and Development of Efficient Bifunctional Catalysts by Tuning the Electronic Properties of Cobalt–Manganese Tungstate for Oxygen Reduction and Evolution Reactions, ChemCatChem 9 (2017) 3681–3690. https://doi.org/10.1002/cctc.201700540.

[54] L. Yao, R. Li, H. Zhang, M. Humayun, X. Xu, Y. Fu, A. Nikiforov, C. Wang, Interface engineering of NiTe@CoFe LDH for highly efficient overall water-splitting, Int. J. Hydrogen Energy 47 (2022) 32394–32404. https://doi.org/10.1016/j.ijhydene.2022.07.135.

[55] K. Brijesh, K. Bindu, D. Shanbhag, H.S. Nagaraja, Chemically prepared Polypyrrole/ZnWO 4 nanocomposite electrodes for electrocatalytic water splitting, Int. J. Hydrogen Energy 44 (2019) 757–767. https://doi.org/10.1016/j.ijhydene.2018.11.022.

[56] B. Jansi Rani, G. Ravi, R. Yuvakkumar, D. Velauthapillai, B. Saravanakumar, E. Sunil Babu, NiWO4@Ni(OH)2 for electrochemical water splitting, in: AIP Conf. Proc., American Institute of Physics Inc., 2020. https://doi.org/10.1063/5.0019371.

[57] U.J. Awan, M.A. Basit, S.I.A. Shah, J. Yong-Xin, H. Zhifu, Minimized OER overpotential via SILAR-based development of g-C3N4/CdS nanocomposite, Appl. Phys. A Mater. Sci. Process. 129 (2023) 1–15. https://doi.org/10.1007/s00339-023-07105-y.

[58] A. Hojatshamami, Ni-Co and Ni-Fe Catalysts for The Oxygen Evolution Reaction in Alkaline Water Electrolysis, (2022). https://hdl.handle.net/11250/3042808 (accessed June 23, 2024).

[59] H. Zeng, Y. Zeng, J. Qi, L. Gu, E. Hong, R. Si, C. Yang, The role of proton dynamics on the catalyst-electrolyte interface in the oxygen evolution reaction, Chinese J. Catal. 43 (2022) 139–147. https://doi.org/10.1016/S1872-2067(21)63909-8.

[60] W. Choi, H.C. Shin, J.M. Kim, J.Y. Choi, W.S. Yoon, Modeling and applications of electrochemical impedance spectroscopy (Eis) for lithium-ion batteries, J. Electrochem. Sci. Technol. 11 (2020) 1–13. https://doi.org/10.33961/jecst.2019.00528.

[61] A. Wieczorek, Y. Liu, H.H. Cho, K. Sivula, Assessing the Charge Carrier Dynamics at Hybrid Interfaces of Organic Photoanodes for Solar Fuels, J. Phys. Chem. Lett. 15 (2024) 6347–6354. https://doi.org/10.1021/acs.jpclett.4c01170.

[62] E. Lebègue, Allen J. Bard, Larry. R. Faulkner, Henry S. White: Electrochemical Methods: Fundamentals and Applications, 3rd edition, Wiley, Transit. Met. Chem. 48 (2023) 433–436. https://doi.org/10.1007/s11243-023-00555-6.

[63] K.S. Bhat, H.S. Nagaraja, Nickel selenide nanostructures as an electrocatalyst for hydrogen evolution reaction, Int. J. Hydrogen Energy 43 (2018) 19851–19863. https://doi.org/10.1016/j.ijhydene.2018.09.018.

[64] R.N. Singh, N.K. Singh, J.P. Singh, Electrocatalytic properties of new active ternary

ferrite film anodes for O2 evolution in alkaline medium, Electrochim. Acta 47 (2002) 3873–3879. https://doi.org/10.1016/S0013-4686(02)00354-7.

[65] L.I. Krishtalik, Kinetics and mechanism of anodic chlorine and oxygen evolution reactions on transition metal oxide electrodes, Electrochim. Acta 26 (1981) 329–337. https://doi.org/10.1016/0013-4686(81)85019-0.

[66] J.O.M. Bockris, T. Otagawa, Mechanism of oxygen evolution on perovskites, J. Phys. Chem. 87 (1983) 2960–2971. https://doi.org/10.1021/j100238a048.

[67] Z. Hu, L. Hao, F. Quan, R. Guo, Recent developments of Co3O4-based materials as catalysts for the oxygen evolution reaction, Catal. Sci. Technol. 12 (2022) 436–461. https://doi.org/10.1039/d1cy01688a.

[68] S. Pal, U. Azad, A. Singh, D. Kumar, R.P.-E. Acta, undefined 2019, Studies on some spinel oxides based electrocatalysts for oxygen evolution and capacitive applications, ElsevierS Pal, UP Azad, AK Singh, D Kumar, R PrakashElectrochimica Acta, 2019•Elsevier (n.d.).